

# Insights into the Main Protease of SARS-CoV-2: Thermodynamic Analysis, Structural Characterization, and the Impact of Inhibitors

Jamie P. Butalewicz,<sup>1</sup> Sarah N. Sipe,<sup>1</sup> Kyle J. Juetten,<sup>1</sup> Virginia K. James,<sup>1</sup> Thomas D. Meek,<sup>2</sup> and Jennifer S. Brodbelt<sup>1\*</sup>

<sup>1</sup>Department of Chemistry, The University of Texas at Austin, Austin, TX, USA

<sup>2</sup>Department of Biochemistry and Biophysics, Texas A&M University, College Station, TX, USA

---

**ABSTRACT:** The global pandemic COVID-19, caused by the severe acute respiratory syndrome coronavirus (SARS-CoV-2), has taken a staggering toll on human health. The main protease of SARS-CoV-2 ( $M^{pro}$ ) is an essential enzyme for coronaviral maturation and is the target of Paxlovid, which is currently the standard-of-care treatment for COVID-19. There remains a need to identify new inhibitors of  $M^{pro}$  as viral resistance to Paxlovid emerges. Here, we report the use of native mass spectrometry coupled with 193-nm ultraviolet photodissociation (UVPD) to structurally characterize  $M^{pro}$  and its interactions with potential inhibitors. Melting temperatures and equilibrium constants, as well as the overall energy landscape, were obtained using variable temperature nano-electrospray ionization (vT-nESI) mass spectrometry, thus providing quantitative evaluation of inhibitor binding on the stability of  $M^{pro}$ . The melting temperature was determined to be approximately 43°C for the dimer and 50°C for the monomer, suggesting an initial thermal dissociation pathway before subsequent unfolding of the monomer species. Thermodynamic parameters extracted from Van't Hoff plots revealed that dimeric complexes containing one of four inhibitors showed enhanced stability through increased melting temperatures as well as overall lower average charge states, giving insight into the basis for potential inhibition mechanisms.

---

## Introduction

The COVID-19 global pandemic, caused by the severe acute respiratory syndrome coronavirus-2 (SARS-CoV-2),<sup>1</sup> emerged from China in December 2019 and has accounted for 761 million worldwide cases with 6.8 million deaths as of September 2023.<sup>2</sup> The availability of vaccines since the end of 2020 has significantly contributed to the control of COVID-19, but as new strains of SARS-CoV-2 continue to emerge,<sup>4</sup> modified vaccines are needed in order to expand their efficacy. The current standard-of-care drug for COVID-19, Paxlovid, is contra-indicated in patients who take other medications that affect CYP3A4 drug metabolism. Point mutations within the target of Paxlovid, the Main protease ( $M^{pro}$ ), have been reported to diminish its efficacy, indicating the development of drug resistance. Accordingly, there remains a need for the discovery of new therapies for COVID-19 despite its apparent dormancy.

SARS-CoV-2 is a positive-sense, single-stranded RNA virus consisting of four structural proteins, an RNA genome, and sixteen nonstructural proteins.<sup>1-4</sup> SARS-CoV-2 is permissive to and infects mammalian cells that express the angiotensin converting enzyme (ACE2)-receptor to which the extracellular spike protein of the virus binds. After fusion with the cellular membrane, proteases within the host cells cleave the spike protein, followed by release of the viral RNA into the cytoplasm.<sup>2,3</sup> Translation of the viral RNA results in two polyproteins, pp1a and pp1ab, which contain nascent forms of the structural proteins and essential enzymes of the mature coronavirus. Among these are two essential proteases, main protease ( $M^{pro}$ ) and papain-like protease ( $PL^{pro}$ ), which catalyze the proteolytic processing of the polyproteins to elaborate the proteases themselves and

other essential enzymes of the virus, including the polymerase RdRp complex which subsequently catalyzes the replication of the viral RNA.<sup>2-4</sup> Because of the importance of understanding the replication and transmission mechanisms of the virus,  $M^{pro}$  has become a focus of research in the treatment and prevention of the virus.

$M^{pro}$  from SARS-CoV-2 is a 67.5 kDa homodimer composed of 34-kDa subunits (**Figure S1**), each of which subunit consists of three distinct domains.<sup>3-5</sup> Domains I (residues 8-101) and II (residues 102-184) contain antiparallel  $\beta$ -barrel structures comprising the active site, while domain III (residues 201-303) contains primarily  $\alpha$ -helices required for dimerization of the protein through generation of salt-bridges.<sup>2,3,6</sup> Domains II and III are connected through an extended loop region, whereas the intersection of domains I and II mark the location of the substrate binding site.<sup>3</sup> Cys145 and His41 constitute the catalytic dyad with the histidine serving as a general acid or base while the cysteine acts as the nucleophilic site.<sup>2,3,7</sup> The structure of this binding pocket as well as the overall sequence of  $M^{pro}$  is highly conserved across the many coronaviruses.<sup>2</sup> Understandably, many pharmaceutical and academic laboratories have sought to identify inhibitors of  $M^{pro}$  that act by either covalent adduction of Cys145 or are non-covalent in nature, for which inhibitory potency has been assessed kinetically using FRET-based peptide substrates, or by thermal shift assays.<sup>5,8-12</sup> While Paxlovid and other  $M^{pro}$  inhibitors which have progressed to clinical evaluation are, in general, peptide analogues that form adducts of Cys145, a greater understanding of how these inhibitors affect the structure and free energy of  $M^{pro}$  would contribute new insights into the mechanism of inhibition.

Recent studies have shown that native mass spectrometry can reveal insights into the stoichiometries of  $M^{pro}$  complexes, and serve as a drug screening assay for a wide variety of potential inhibitors.<sup>5,8,9,13</sup> For example, in one study native MS was used to determine the dissociation constant of  $M^{pro}$  ( $0.14 \pm 0.03 \mu M$ ) based on the monomer/dimer equilibrium and to monitor substrate turnover rates in the presence of small molecule inhibitors.<sup>14</sup> Combining these types of native MS methods with variable temperature electrospray ionization<sup>14-16</sup> or ion mobility spectrometry<sup>17-20</sup> offers the potential to reveal additional thermodynamic and structural characteristics of  $M^{pro}$  and inhibitor complexes.

Determination of the thermodynamic properties of proteins and protein complexes is essential for understanding their structures, conformational dynamics, interactions, and functions. The strength of the various interactions can be studied through the Gibbs free energy ( $\Delta G$ ) along with its composite enthalpy ( $\Delta H$ ) and entropy ( $\Delta S$ ) contributions. Proteins are stabilized through their networks of hydrogen bonding and electrostatic interactions. As a system is stabilized, the enthalpy will be low (negative) and favorable, whereas the entropy will be unfavorable as it reflects the configurational freedom of the protein.<sup>15,21,22</sup> The entropy describes structuring of the protein and conformational organization, while the enthalpy gives insights into binding modes, including intra- and intermolecular interactions within the protein.<sup>15,22</sup> While the protein structure can be studied through many biophysical methods, the measurement of thermodynamic parameters provides a quantitative description of the energetics of the system.

Variable temperature nano-electrospray ionization (vT-nESI) mass spectrometry has recently gained popularity to probe protein structure and its destabilization during heating or cooling.<sup>14,16,23,23-25</sup> While there are numerous custom-built variable temperature ionization sources,<sup>16,21,24,26</sup> they all effectively feature a heater that surrounds the sample solution to uniformly control the temperature prior to electrospray ionization and MS analysis. Thermal denaturation of a protein is observed through a shift to higher charge states in the ESI mass spectra; the change in charge state distribution arises from an increase in exposed surface area upon protein unfolding resulting in greater accessibility of protonation sites. By incrementally increasing the temperature of the solution and allowing time for temperature equilibration, the average protein charge state at each temperature is used to generate a melting curve and subsequently derive a melting point. Moreover, thermodynamic properties, including  $\Delta G$ ,  $\Delta H$ , and  $T\Delta S$ , can be extracted by Van't Hoff analysis.

Concurrent to measurement of thermodynamic properties, tandem mass spectrometry methods, such as ultraviolet photodissociation (UVPD), have been extensively used to characterize native protein structures.<sup>27-30</sup> UVPD affords high-level sequence coverage of both denatured and native-like proteins through high-energy photon activation, revealing both primary sequence information as well as regions of higher order structure.<sup>28,30,31</sup> In this work, we report the structural and thermodynamic characterization of  $M^{pro}$  from SARS-CoV-2 bound with several known inhibitors through high resolution mass spectrometry in conjunction

with 193 nm UVPD, vT-nESI, and ion mobility measurements.

## Methods and Materials

**Materials.**  $M^{pro}$  was produced and characterized in-house as described elsewhere by Mellott et al 2021<sup>32</sup> and its sequence is shown in **Figure S1**. Additional details are provided in **Supporting Information**.<sup>4,33</sup> Kinetic analysis of this preparation of  $M^{pro}$  (25 nM) using the FRET-based peptide substrate Abz-SAVLQ\*SGFRK(DNP)-NH<sub>2</sub> resulted in kinetic parameters of:  $K_m = 66 \pm 9 \mu M$ ,  $k_{cat} = 4.9 \pm 0.4 s^{-1}$  and  $k_{cat}/K_m = 74,000 M^{-1}s^{-1}$  acquired at pH 7.5 and at 25°C.  $M^{pro}$  was exchanged into 100 mM ammonium acetate using P-6 Bio-Spin columns (Bio-Rad Laboratories, Hercules, CA), and diluted to 5  $\mu M$  for all experiments unless noted otherwise.  $M^{pro}$  inhibitors boceprevir, 11A, 11B, and GC376 were purchased from Cayman Chemical (Ann Arbor, MI) and used as received (see structures and MS1 spectra in **Figure S2**). Inhibitors were diluted to 5  $\mu M$  in 100 mM ammonium acetate (pH ~7) for individual analysis. For binding experiments,  $M^{pro}$  was diluted to 10  $\mu M$  in 100 mM ammonium acetate with 5x concentration of inhibitor added, and allowed to incubate at room temperature for one hour before MS analysis. All samples were loaded into gold/palladium-coated ESI emitters pulled in-house.

**Instrumentation.** A Q-Exactive HF-X BioPharma Orbitrap mass spectrometer (Thermo Fisher Scientific, Bremen) modified for 193 nm UVPD with a Coherent Excistar ArF excimer laser (Santa Cruz, CA) was used for all experiments. UVPD was performed in the HCD cell as described previously<sup>34-36</sup> using an Orbitrap resolution of 240,000 at  $m/z$  200. Proteins were activated using a single laser pulse of 1.5 mJ, and all spectra were collected in triplicate.

A variable temperature nano-electrospray ionization source was built based on a design described elsewhere.<sup>16</sup> The detailed protocol for the variable temperature ESI measurements and calculation of thermodynamic parameters are provided in **Supporting Information**.

For ion mobility (IM) experiments, an atmospheric pressure drift tube was mounted to the front end of the mass spectrometer. The drift tube was constructed as described previously,<sup>37,38</sup> and additional details are provided in **Supporting Information**. For all experiments, three replicate sweeps were collected and extracted ion chromatograms (XICs) averaged prior to Fourier transformation and processing.

Circular dichroism (CD) spectra were collected on a Jasco J-815 spectrometer using a wavelength range of 190 nm to 260 nm and scan rate of 50 nm/min.  $M^{pro}$  was diluted to 2  $\mu M$  using 50 mM ammonium acetate and spectra were background subtracted using a 50 mM ammonium acetate solution. 10 scans were collected and averaged at each temperature setpoint. Absorption at 222 nm, which represents  $\alpha$ -helical character in a protein,<sup>39,40</sup> was used for subsequent analysis. CD spectra are shown in **Figure S3**.

**Data Analysis** Native mass spectra were deconvoluted and identified using Unidec,<sup>41</sup> while UVPD mass spectra were deconvoluted using Xtract in QualBrowser. Deconvoluted spectra were further analyzed using MS-TAFI<sup>42</sup> to identify fragment ion types, generate abundance maps, and compare sequence coverages obtained over multiple

experiments. UVPD fragments were normalized to the TIC of the fragmentation spectrum and identified in two out of the three replicates in order to be used for further analysis. Fragmentation data was mapped to the protein crystal structure (PDB: 7CAM) using PyMOL (PyMOL Molecular Graphics System, version 2.5.2 Schrödinger, LLC). All ion mobility data was processed using extracted ion chromatograms from the IM-MS experiments using a custom MATLAB script.

## Results and Discussion

**Ion Mobility and UVPD Fragmentation Associate Dimer Interface with Protein Activity.** The native-like structure of dimeric  $M^{pro}$  was studied through a variety of mass spectrometry methods, including vT-nESI-MS, drift tube IM, and UVPD.  $M^{pro}$  is a homodimer comprised of two identical subunits, each of which contain three distinct domains (**Figure S1**) and a binding pocket in a cleft between domains I and II comprised of a key catalytic dyad between Cys145 and His41.<sup>3-5</sup> The ESI mass spectrum of  $M^{pro}$  in a native-like solution of high ionic strength (100 mM ammonium acetate, pH = ~7.0) is shown in **Figure 1A**. The dimeric species is dominant and is observed in a narrow charge-state distribution centered around the 16+ charge state. The monomer (10+ and 11+ charge states) are also observed in lower abundance, possible due to some disassembly of the dimer during the ESI process. As seen in **Figure 1**, the dimers do not contain twice as many charges as the monomers, consistent with the expectation that the dimer interface is not surface-accessible and thus is partially shielded from protonation. When the dimer dissociates in bulk solution or in the ESI droplets, previously inaccessible basic sites involved in the interface region are exposed and the progeny monomers retain more protons on average per molecule than the dimer. Deconvolution of the mass spectrum yielded a mass of 67,554 Da for the dimer and 33,796 Da for the monomer (**Figure S1**).

To ascertain the relative molecular sizes of the  $M^{pro}$  monomers and dimers, the collision cross sections (CCS) of the ions were measured using ambient-pressure drift-tube ion mobility spectrometry (DTIMS). The CCS represents the rotationally averaged molecular area of a protein, correlating with its degree of compactness or unfolding as influenced by particular tertiary or quaternary structural features. The mass spectra obtained after the ions traverse the drift tube are shown in **Figure S4**. The charge states of the monomers are 9+ to 11+ and dimers are 13+ to 16+. Somewhat lower charge state distributions are observed compared to those in **Figure 1**, a known outcome owing to the longer desolvation region and therefore extended time spent at ambient pressure.<sup>18,43</sup> The CCSs of the dimers and monomers are derived from the mobility-based chromatograms (arrival time distributions) of the observed charge states shown in **Figure 1B**. The CCS of the dimers ranged from  $3882 \pm 10 \text{ \AA}^2$  (13+) to  $4033 \pm 20 \text{ \AA}^2$  (15+), and the CCS of the monomers were  $2583 \pm 17 \text{ \AA}^2$  (9+) and  $2625 \pm 10 \text{ \AA}^2$  (10+). Applying the Rosetta Projection Approximation using the Rough Circular Shapes (PARCS) algorithm<sup>44,45</sup> on crystal structures of the native apo monomer (2H2Z) and dimer (7CAM), the CCS values were predicted to be  $2654 \text{ \AA}^2$  and  $3970 \text{ \AA}^2$ , respectively. The values are in good agreement with the ones measured by ion mobility and provide

evidence that compact, native-like structures are preserved upon nESI.

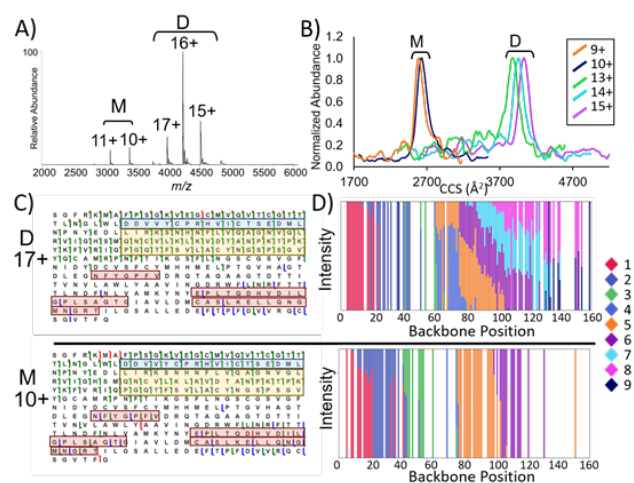


**Figure 1.** A) Native mass spectrum of  $M^{pro}$  displaying both dimers (D) and monomers (M) acquired at 250C. B) Collision cross-section (CCS) measurements of various charge states of dimers (13+ (green), 14+ (blue), 15+ (purple)) and monomers (9+ (orange) and 10+ (navy)) of  $M^{pro}$  collected using an ambient pressure drift tube ion mobility spectrometer. C) Sequence coverage maps generated for the dimer (16+) and monomer (10+) by UVPD (1 pulse, 1.5 mJ per pulse). The pink- and blue-shaded boxes highlight sequence regions of the monomer that exhibit increased fragmentation relative to the dimer. The blue-shaded box overlaps with a sequence region in the active site and binding pocket, whereas the pink regions are located within domains II and III. The gold shaded box outlines a region spanning residues 57-125 (parts of Domains I and II) in which fragmentation is notably enhanced for the dimer. (D) Charge site localization based on charge states of a and a+1 fragment ions originating from backbone cleavages spanning residues 1-160 for the dimer and monomer.

UVPD was performed on the monomer (10+) and dimer (17+) to evaluate the impact of the dimer interface on the fragmentation of  $M^{pro}$ . Representative UVPD mass spectra are shown in **Figure S5**, and identified fragment ions and their corresponding normalized abundances are summarized in **Table S1**. Sequence coverage of the dimer (17+) was 42% with fragmentation primarily occurring in the N-terminal region containing domain I (**Figure 1C**). Because the majority of the non-covalent interactions that stabilize the dimer interface originate from residues in domain III (see **Figure S1B**), minimal fragmentation is expected in this region owing to the prevalence of salt bridges and hydrogen bonding interactions that both stabilize the interface and suppress the separation/release of fragment ions even if individual backbone bonds are cleaved by UVPD. The sequence coverage of the monomer (10+) was also 42%; however, more extensive fragmentation occurred from backbone cleavages of domain III and fewer fragment ions originated from backbone cleavages of domain I. Minimal fragmentation of the middle sequence section, domain II, of both the monomer and dimer is not unique to this protein as top-down characterization of intact proteins by MS/MS

inevitably results in diminished coverage in the mid-sections of proteins. The large sizes of fragment ions produced from the mid-regions of proteins are less readily identified owing to their  $m/z$  overlap with other ions, particularly abundant non-dissociated precursor ions, which degrades the resolution of their isotope distributions and impedes confident assignment.<sup>46</sup>

Despite the identical numerical values of the sequence coverages (42%) for the dimer and monomer, fragmentation of certain sequence sections differs significantly, as highlighted by the shaded sequence segments in **Figure 1C**. The sequence segments shaded in pink and blue in **Figure 1C** designate regions for which a greater array of fragment ions are produced for the monomer, suggesting that these regions are less stabilized by intermolecular interactions, enhancing the separation and release of fragment ions upon backbone cleavage by UVPD. The blue shaded segment encompasses one portion of the active site of the protein. Salt-bridges in this region stabilize the dimer and create a more rigid structure to organize the active site, suppressing UVPD.<sup>4,7,47,48</sup> This result supports previous accounts of the monomer and dimer activity of  $M^{pro}$  which found that the greatest catalytic activity is observed through dimerization when an inhibitor can bind at least one active site of the protein complex whereas the monomer itself shows minimal activity.<sup>48</sup> The active site loses its structure and therefore functionality upon disassembly of the dimer, thus facilitating fragmentation of this section of the monomeric protein by UVPD. Additionally, the region spanning residues ~57-125 is shaded in gold on the sequence maps in **Figure 1C** and shows notably enhanced fragmentation of the dimer relative to the monomer. We speculated that this enhancement of fragmentation of the dimeric structure corresponds to a structural rearrangement as the dimer dissociates and unfolds, exposing previously buried residues within the active site.

Charge site analysis was performed on the N-terminal region of the protein (residues 1 – 160) based on analysis of the charge states of all  $a$ -type fragment ions ( $a$  and  $a_n + 1$ ) generated by UVPD.<sup>49,50</sup> Charge site analysis provides insight on the locations of charges (protons) along a protein's primary sequence, generally corresponding to solvent accessibility of the protein during electrospray ionization.<sup>49,50</sup> **Figure 1D** shows that fragments of the monomer (10+) only contain up to six charges, suggesting the additional four charges are localized to the C-terminal domain spanning residues 160-303. The observed charge states of the fragments generated from the monomer exhibit relatively discrete changes along the primary sequence, allowing a means to systematically assign general charge site locations. For example, backbone positions Val20, Val42, Ile78, and Lys102 are likely protonated or within one residue of protonation sites corresponding to the sharp shifts in fragment ion charge states. In contrast, fragments containing up to nine charges are observed upon dissociation of the dimer (17+) by UVPD, and the step changes between charge sites are much more "blurred" in the region spanning residues 60 to 140 (*e.g.* many of the fragment ions are produced in multiple charge states, as exemplified by the  $a_{89}$  and  $a_{95} + 1$  ion series displaying 6+, 7+, and 8+ charge states for the dimer and only 6+ charge state for the monomer). These

observations suggested that either the C-terminal domain III is unusually depleted of charge for the dimer or that extensive hydrogen bonding interactions and salt-bridges of the dimer interface allow substantial charge migration.<sup>51</sup> Some basic residues in the interface region are less accessible in the dimer than the monomer, making them less prone to protonation during the ESI process, thereby accounting for the lower charge density of the dimer than the monomer. Additionally, the detection of the same fragment ions in three or four different charge states for the dimer may indicate there are several different protonated forms prior to UVPD.

**Thermal denaturation reveals both disassembly and unfolding of the dimer at elevated temperatures.** Variable temperature nESI of  $M^{pro}$  was undertaken to study the thermal decomposition as a function of solution temperature. These variable temperature measurements also allow thermodynamic analysis, as described later. **Figure 2A** shows mass spectra of  $M^{pro}$  acquired at 25°C (room temperature) and 50°C. An entire series of mass spectra collected at other solution temperatures is shown in **Figure S6**. The spectrum acquired at 50°C reveals a significant enhancement in the abundance of monomers and a notable shift in the charge state distribution of the dimers. Based on summation of the peak abundances (based on peak height) for the different charge states of the monomers and dimers, the average charge states were calculated as a function of solution temperature (**Figure 2B**).

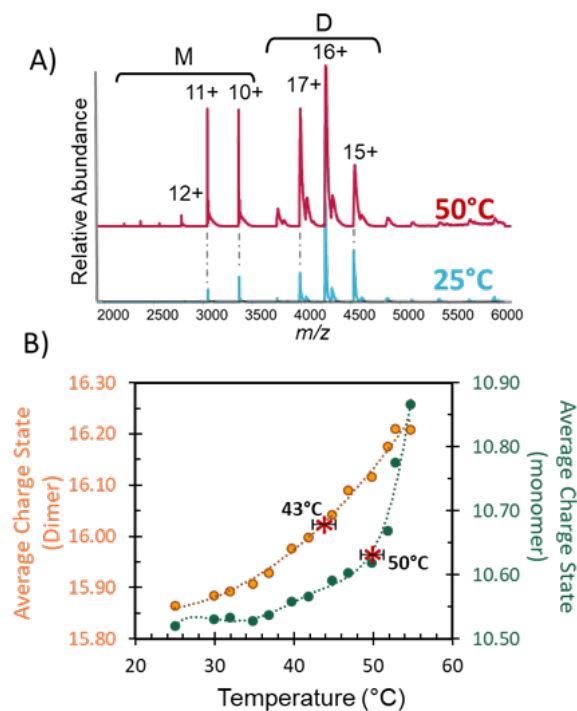


**Figure 2.** A) Native MS1 spectrum of  $M^{pro}$  acquired at 25°C (blue) and 55°C (red). B) Average charge state of the monomers and dimers as a function of temperature. The monomer is shown in green (right axis) while the dimer is shown in orange (left axis). The melting temperature for dimer and monomer species correspond to inflection points and are highlighted with red asterisks.

The average charge state of the dimers increased from approximately 15.8 at 25°C to 16.2 at 55°C with the emergence of 18+ charge state around 55°C indicating unfolding or elongation of the dimer, exposing additional ionizable residues. The increase in the abundances of the monomers as the solution temperature is raised indicated dimer dissociation. Highly charged monomers, 12+ to 15+, appeared in low abundance at the higher temperatures as well, shifting the average charge state of the monomer from approximately 10.5 to 10.9. Even greater increases in temperature lead to apparent protein aggregation and loss of ion signal. A comparison to the CD data collected at various temperatures is shown in **Figure S7**. The average melting temperature of the dimer species was determined to be approximately 43°C, while it was 50°C for the monomer. In general,  $M^{\text{pro}}$  exhibits both unfolding and disassembly pathways when subjected to thermal denaturation.

The 12+ charge state of the monomer at 50°C was chosen for subsequent characterization by UVPD as it is not present at room temperature, designating this charge state to be exclusively a product of thermal denaturation. **Figure 3A** shows the fragmentation of the protein based on the abundances of fragment ions originating from cleavages of each backbone position for the 17+ dimer (previously shown as a sequence map in **Figure 1C**) at room temperature (blue) and the thermally denatured monomer (12+) (red, values shown on an inverted scale). Regions of increased fragmentation of the thermally denatured monomer relative to the dimer are highlighted with a pink-shaded box while regions that exhibit suppressed fragmentation upon thermal denaturation are highlighted in a blue-shaded box. These highlighted regions are color-coded on the crystal structure of the dimer in **Figure 3B**. It is expected that the thermally denatured monomer would exhibit increased fragmentation in domain III of the protein (interface region). The loss of the subunit interface disrupts many of the hydrogen bonds and salt bridges in this region, promoting greater fragmentation efficiency of the highly  $\alpha$ -helical domain III. Similar to the fragmentation of the monomer at room temperature, the thermally denatured monomer displayed greater fragmentation in the active site region (residues 40-180) than any other section of the protein, likely due to increased conformational flexibility of the binding pocket and loss of functionality. Fragmentation of the region comprised of residues ~60-140 appeared to be even more enhanced for the dimer compared to the thermally denatured monomer. This region contains primarily  $\beta$ -sheet secondary structure, a class of secondary structure which has previously been reported to exhibit high melting temperatures as well as the ability to stabilize intermediate structures at high temperature.<sup>52-55</sup> It is possible that these properties of the  $\beta$ -sheet region afford greater stability during the thermal denaturation experiments while the surrounding areas undergo more extensive fragmentation. If the protein did not aggregate at ~65°C, it is possible that further unfolding events of this  $\beta$ -strand region might have been observed at higher temperatures.

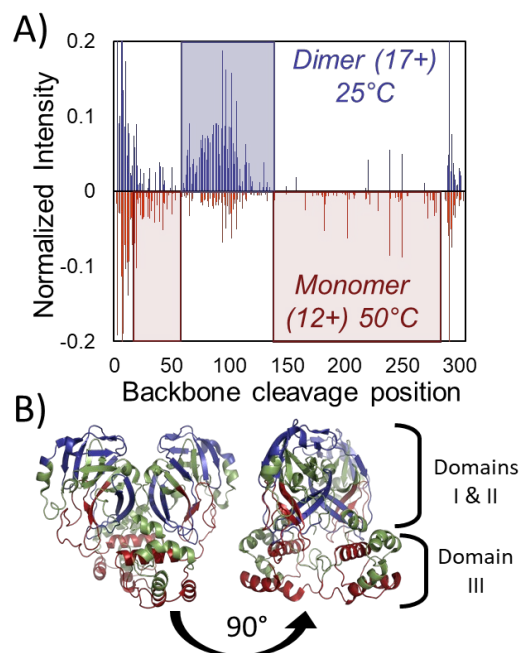


**Figure 3.** UVPD was performed on the 17+ dimer at room temperature and the 12+ monomer at elevated temperature. Fragments identified and normalized by MS-TAFI were plotted according to the backbone position that was cleaved with the monomer intensities shown on an inverted scale. (A) Regions displaying enhancement or suppression of fragmentation between the monomer and dimer are denoted by shaded boxes: red for enhanced fragmentation of the monomer at 50°C and blue for enhanced fragmentation of the dimer at 25°C. (B) These regions of differences in fragmentation were mapped on the crystal structure of dimeric  $M^{\text{pro}}$  (PDB: 7CAM) where green is the standard color of the protein and red/blue corresponds to the regions shaded in A.

**The Dimeric  $M^{\text{pro}}$  Dissociation Pathway is Entropically Driven while Unfolding of the Monomer is Enthalpically Driven.** Thermodynamic analysis of  $M^{\text{pro}}$  was undertaken using the variable temperature ESI mass spectra acquired across from 25°C to 70°C in 2-5°C increments (**Figure S6**). The resulting data was used to generate Van't Hoff plots (**Figure S8**). The Gibbs free energy ( $\Delta G$ ), enthalpy ( $\Delta H$ ), and entropy ( $-T\Delta S$ ) were extracted from the Van't Hoff plots for each charge state of monomer and dimer at 25°C (**Figure 4**).

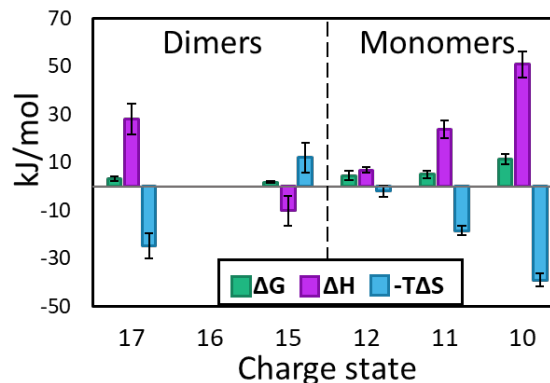


**Figure 4.** Thermodynamic parameters for the dimer (17+ to 15+) and monomer (12+ to 10+) of  $M^{\text{pro}}$  calculated at 25°C using the dimer (16+) as the reference.

An overall trend of decreasing enthalpy with increasing charge state is observed for the monomers, suggesting stabilization of thermally unfolded intermediates through the generation of new hydrogen bonds or intramolecular salt bridges from previously buried residues. As the protein undergoes denaturation during the temperature ramp, thus unfolding and becoming more highly charged, rearrangement of the intramolecular interactions occurs. The decreasing enthalpy suggested that the overall structure of each subsequent charged species is more energetically stable than the previous, which typically denotes favorable or spontaneous reactions. Interestingly, the enthalpy of the dimer increases with charge state. This result suggested that while the unfolding of the monomer is an enthalpically driven process, the dimer is more resistant to unfolding owing to the greater number of non-covalent interactions that must be disrupted (i.e., more bonds are being broken than formed). An overall trend of increasing  $-\Delta S$  (or decreasing  $\Delta S$ , entropy) is observed as the charge state of the monomer increases. This decrease in entropy corresponds to the configurational freedom of the protein, and further supports that the 'unfolded' monomers engage in new intramolecular interactions for stabilization, consistent with the concurrent decrease in enthalpy. Again, as the protein denatures and becomes more highly charged, it can adopt a more energetically stable conformation than previously. Comparison of the entropy of the dimer in the 15+ charge state (as it is likely not a product of thermally induced unfolding) to that of the monomer in the 10+ charge state (which is likely the direct product of dimer dissociation and not unfolding) suggests that thermal dissociation of the dimer may be an entropically driven process. The free energy changes little for the different charge states of the dimers, demonstrating the balance of entropically and enthalpically driven unfolding and dissociation pathways throughout the thermal denaturation process.

**Inhibitor Binding Increases the Thermal Stability and Formation of the M<sup>pro</sup> Dimer.** The impact of inhibitor binding on the fragmentation patterns, collision cross sections,

and thermodynamic parameters of M<sup>pro</sup> was evaluated using native mass spectrometry in conjunction with ion mobility and variable temperature ESI analysis. Four inhibitors were evaluated: 11A,<sup>56,57</sup> 11B,<sup>56,57</sup> boceprevir,<sup>9,10</sup> and GC-375.<sup>10</sup> These inhibitors were chosen due to their known modes of binding and inhibition of M<sup>pro</sup>. 11A and 11B were found to be potent covalent inhibitors of M<sup>pro</sup> (respective IC<sub>50</sub> values of  $0.53 \pm 0.005 \mu\text{M}$  and  $0.040 \pm 0.002 \mu\text{M}$ ).<sup>56</sup>

These two inhibitors feature an aldehyde warhead that forms a thiohemiacetal adduct with Cys145 in M<sup>pro</sup>. The only difference between the inhibitors is the replacement of the cyclohexane ring of 11A with a 3-fluorophenyl group of 11B; the 3-fluorophenyl group interacts with Gln189 within the active site of the protein. GC-376 (IC<sub>50</sub> of  $0.15 \pm 0.03 \mu\text{M}$ )<sup>12</sup> contains a bisulfite-adduct of a C-terminal aldehyde, which apparently is removed during the time course of inhibition of M<sup>pro</sup> as a thiohemiacetal adduct is also formed with Cys145 of M<sup>pro</sup>. This inhibitor engages in hydrogen bonds within the active site of the protein, mimicking a natural peptide substrate of M<sup>pro</sup>.<sup>9,12</sup> Boceprevir is an FDA-approved drug used to treat the hepatitis C virus.<sup>57</sup> As with other inhibitors of M<sup>pro</sup>, in addition to the thiohemiacetal adduct boceprevir establishes with Cys145, the inhibitor forms additional non-covalent interactions with His41, Gly143, His164 and Gln166 and displayed an IC<sub>50</sub> value of  $1.90 \mu\text{M}$ .<sup>9,10</sup> **Figure 5A** shows the native spectra acquired for solutions containing M<sup>pro</sup> and each of the inhibitors. For all four inhibitors, complexes of the type D•I and D•2I were predominant (D = dimer, I = inhibitor), consistent with prior studies of inhibitor binding of M<sup>pro</sup>.<sup>9</sup> Monomeric complexes of the type M•I were not observed (M = monomer).

CCS values were determined for each D•I complex by drift tube ion mobility measurements. CCS calculations from arrival time distributions (ATD) are shown in **Figure 5B** for the apo and holo dimers in the 14+ and 15+ charge states. The drift tube could not resolve complexes with 1 vs. 2 inhibitors bound, so the estimated CCS values are a composite of both D•I and D•2I, shown in **Figure S9**. The CCS values of the holo dimers were  $4265 \text{ \AA}^2$  (15+) and  $4222 \text{ \AA}^2$  (14+), and the corresponding values for the apo dimers

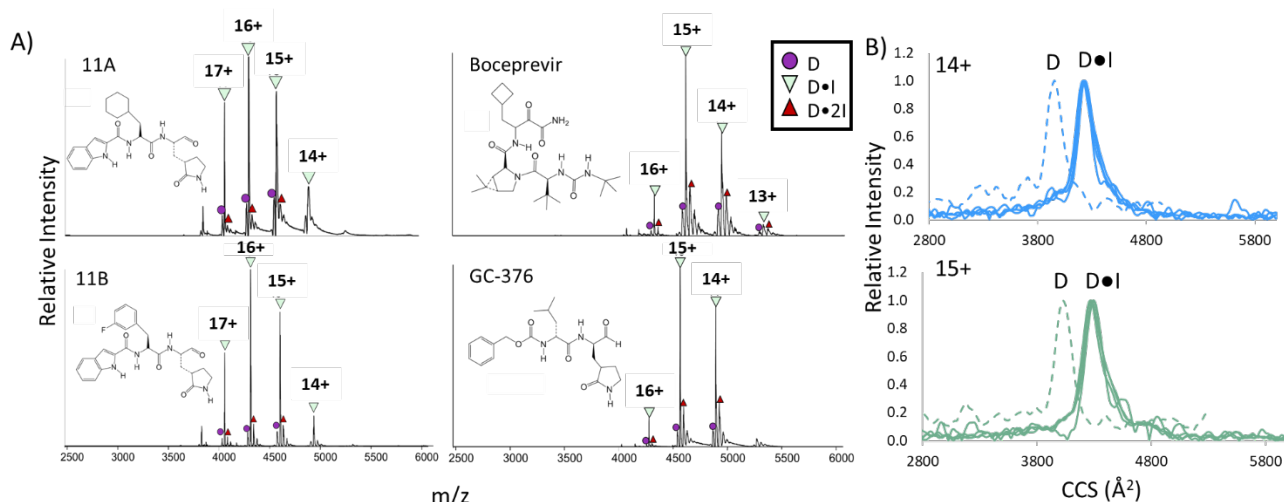


**Figure 5. A)** MS1 spectra at room temperature of solutions containing M<sup>pro</sup> with each inhibitor (I): 11A, 11B, boceprevir, or GC-376 (active form). All abundant complexes are M<sup>pro</sup> dimers. **B)** collision cross sections of the 14+ (solid blue traces) and 15+ (solid green traces) charge states of each of the 2M<sup>pro</sup>•inhibitor complexes (D•I) (all overlaid for each of the four inhibitors) and apo dimer (D) (dashed traces).

were 4033 Å<sup>2</sup> (15+) and 4023 Å<sup>2</sup> (14+), indicating an increase in size of approximately 200 Å<sup>2</sup> upon binding of the inhibitor, presumably owing to widening of the binding pocket region. The CCS values calculated using the PARCS algorithm<sup>44,45</sup> for D•2boceprevir (PDB:7BRP) and D•2GC-376 (PDB: 7D1M) are 3933 Å<sup>2</sup> and 3972 Å<sup>2</sup>, respectively; both essentially the same as the CCS value calculated for the apo dimer (3970 Å<sup>2</sup>, PDB:7CAM). While the PARCS CCS calculation of the apo dimer is consistent with the value experimentally measured for the various charge states of the apo dimer based on ion mobility in the present study, the deviation in agreement for the holo dimer species suggested that inhibitor binding may not generate as compact a structure in the gas-phase when compared to the theoretical structures.

As done for the apo dimers, vT-nESI measurements were undertaken on each D•I complex to allow calculation of thermodynamic parameters. The resulting Van't Hoff plots are shown in **Figure S8**, and **Figure 6** summarizes the thermodynamic parameters for each of the complexes in various charge states. The charge state of the reference species was selected based on the charge state that exhibited the least variation in abundance throughout the temperature range: 16+ for D•I complexes containing 11A and 11B and 15+ for the complexes containing boceprevir and GC-376. The thermodynamic parameters for the complexes containing 11A and 11B are similar, an outcome consistent with the similar structures of the inhibitors which also follow similar inhibitory mechanisms. The process of thermal denaturation for these two complexes follows an entropically driven pathway, evidenced by the increase in entropy and decrease in enthalpy with each charge state. There is no thermal dissociation observed for these complexes, and instead aggregation occurs around 75°C, which contrasts with the low melting temperature and disassembly of apo M<sup>pro</sup> dimer discussed earlier. Binding of 11A or 11B decreased the enthalpy of dimeric M<sup>pro</sup>, likely due to the increase in intramolecular interactions that induces greater thermal stability. A plot of the average charge state of each of the D•I complexes as a function of solution temperature in comparison to the apo dimer shows the impact of the inhibitor on the stability of M<sup>pro</sup> (**Figure 6B**). While the M<sup>pro</sup> dimer displayed little change in its charge state (averaging ~16.2) over a wide temperature range, binding of any of the inhibitors decreased the average charge state considerably at 25°C (averaging 14.7-15.0 depending on the inhibitor). This decrease in average charge state for the D•I complexes likely suggested that basic residues previously serving as potential protonation sites near the binding pocket of the complex are involved with interactions and binding of the inhibitor within the same spatial region. As the solution temperature increases, both D•11A and D•11B complexes exhibited a significant increase in average charge state, indicative of unfolding. The temperature-dependent curves for the D•boceprevir and D•GC-376 complexes are much flatter, implying that these inhibitors stabilize the dimer. When comparing the inherent stability of these inhibitor complexes with published values of K<sub>i</sub> and IC<sub>50</sub> for the same species, D•boceprevir and D•GC-376 display greater inhibition values than 11A and 11B suggesting that thermostability and inhibition may be correlated factors that could improve further inhibitor discovery and screening.

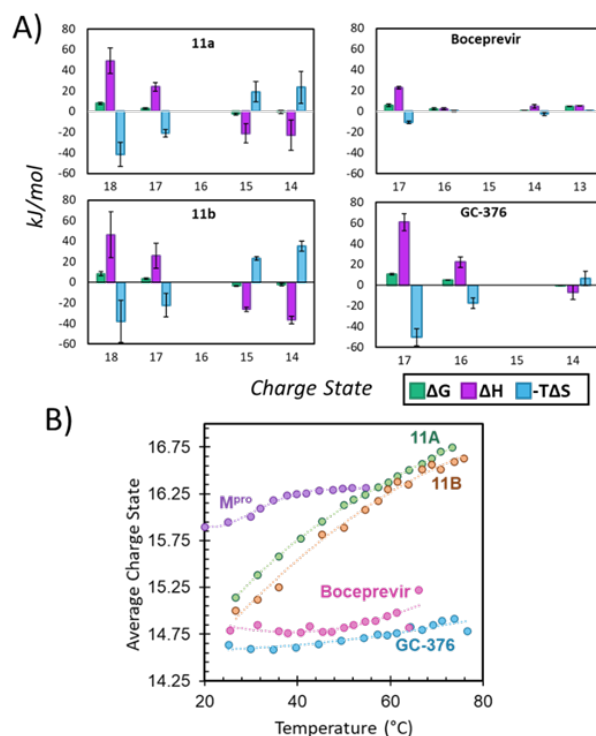


**Figure 6. A)** Thermodynamic parameters for each of the D•I complexes at 25°C. **B)** Average charge state for each of the D•I complexes and apo M<sup>pro</sup> dimer.

The inhibitor GC-376 (IC<sub>50</sub> = 0.19 ± 0.04 μM) is a dipeptide analogue containing a warhead comprised of a bisulfite-masked aldehyde which elaborates to an aldehyde prior to or upon binding to M<sup>pro</sup>.<sup>16</sup> The Cbz-Leu-2-oxo-pyrrolidin-2-yl-alanyl scaffold of this inhibitor resembles the Leu-Gln sequences that comprise cleavage sites in the substrates of this protease. The effectiveness of GC-376 is attributed to its extensive interactions with M<sup>pro</sup> in the binding pocket.<sup>9</sup> The high binding affinity increases the thermal stability of the complex, ultimately aggregating around 80°C. As shown in **Figure 6A**, thermal unfolding of the D•GC-376 complex mirrors the trends in thermodynamic parameters obtained for the 11A/11B complexes. While the complex exhibited a low enthalpy likely due to the extensive interactions with the inhibitor in the binding pocket, it appeared to thermally unfold through an entropically driven process.

The M<sup>pro</sup>•boceprevir complex exhibited the greatest difference in thermodynamic parameters compared to the other complexes. Among the 13+ to 16+ charge states, there is a ≤5 kJ/mol difference for each thermodynamic parameter, and the complex is very stable as evidenced by the minimal change in charge state distributions over a range of temperatures. While inhibitors like GC-376 utilize a bisulfite reactive warhead to covalently affix within the active site of M<sup>pro</sup>, boceprevir has an α-ketoamide group and a notably different chemical structure.<sup>9,10</sup> The interactions of this inhibitor in the active site of M<sup>pro</sup> have been detailed elsewhere,<sup>2-4,8,9,11</sup> featuring strong hydrogen bonding interactions of the amide backbone of boceprevir with M<sup>pro</sup> residues His41, Gly143, His164, and Glu166. Notably, the hydrophobic side chains of boceprevir can be accommodated

to fit into this binding pocket contrary to previous notions that only hydrophilic residues could be accommodated,<sup>5,10</sup> rationalizing the significant stability boceprevir confers to the M<sup>pro</sup> dimer.

### Conclusions

The structure of M<sup>pro</sup> was characterized through native mass spectrometry and drift tube ion mobility to elucidate the collision cross sections of its dimer and monomer species as well as probe the influence of the active site on the structure and functionality of the protease. The dimer retained a more rigid, compact structure around its active site, whereas the monomer is more unstructured in this region owing to unfolding and absence of many intramolecular interactions as indicated by UVPD data. While published X-ray and cryo-EM structures have depicted this intact dimer protease structure, UVPD has provided additional details about the regions that may undergo disruption of non-covalent interactions and lose structural organization based on the observation of increased fragmentation around the active site. vT-ESI studies determined a melting temperature of approximately 43°C ± 2°C for the dimer and 50°C ± 2°C for the monomer, suggesting an initial thermal dissociation pathway before subsequent unfolding of the monomer species. Thermodynamic parameters extracted from Van't Hoff plots revealed that dissociation of the dimeric complex was driven through an entropic process, whereas thermal unfolding was consistent with an enthalpically-promoted process. Understanding the thermodynamics of M<sup>pro</sup> provides insights into the overall stability, folding and unfolding pathways, and interactions of the protease which may be critical for its role in cellular processes and to accelerate targeted drug development. vT-ESI analysis of the dimeric complexes containing one of four inhibitors showed enhanced stability based on increased melting temperatures as well as overall lower average charge states. While these small molecules have been shown previously to inhibit M<sup>pro</sup>, mass spectrometry has allowed determination of thermodynamic parameters for each M<sup>pro</sup>•inhibitor complex. While no thermal dissociation is observed when M<sup>pro</sup> is bound to an inhibitor, differing pathways of unfolding and stability can be seen through the four inhibitors tested. While M<sup>pro</sup>•11A and M<sup>pro</sup>•11B demonstrate entropically driven unfolding mechanisms, the boceprevir and GC-376 complexes follow more enthalpically driven pathways.

### Acknowledgements

This research was supported by the National Institutes of Health (R35GM139658) and the Robert A. Welch Foundation [F-1155]. The TOC graphic was created using Biorender.com.

### REFERENCES

- (1) Gorbalenya, A. E.; Baker, S. C.; Baric, R. S.; de Groot, R. J.; Drosten, C.; Gulyaeva, A. A.; Haagmans, B. L.; Lauber, C.; Leontovich, A. M.; Neuman, B. W.; Penzar, D.; Perlman, S.; Poon, L. L. M.; Samborskiy, D. V.; Sidorov, I. A.; Sola, I.; Ziebuhr, J.; Coronaviridae Study Group of the International Committee on Taxonomy of Viruses. The Species Severe Acute Respiratory Syndrome-Related Coronavirus: Classifying 2019-nCoV and Naming It SARS-CoV-2. *Nat. Microbiol.* **2020**, *5* (4), 536–544. <https://doi.org/10.1038/s41564-020-0695-z>.
- (2) Yang, H.; Yang, J. A Review of the Latest Research on M<sup>pro</sup> Targeting SARS-COV Inhibitors. *RSC Med. Chem.* **2021**, *12* (7), 1026–1036. <https://doi.org/10.1039/D1MD00066G>.
- (3) Jin, Z.; Du, X.; Xu, Y.; Deng, Y.; Liu, M.; Zhao, Y.; Zhang, B.; Li, X.; Zhang, L.; Peng, C.; Duan, Y.; Yu, J.; Wang, L.; Yang, K.; Liu, F.; Jiang, R.; Yang, X.; You, T.; Liu, X.; Yang, X.; Bai, F.; Liu, H.; Liu, X.; Guddat, L. W.; Xu, W.; Xiao, G.; Qin, C.; Shi, Z.; Jiang, H.; Rao, Z.; Yang, H. Structure of M<sup>pro</sup> from SARS-CoV-2 and Discovery of Its Inhibitors. *Nature* **2020**, *582* (7811), 289–293. <https://doi.org/10.1038/s41586-020-2223-y>.
- (4) Zhang, L.; Lin, D.; Sun, X.; Curth, U.; Drosten, C.; Sauerhering, L.; Becker, S.; Rox, K.; Hilgenfeld, R. Crystal Structure of SARS-CoV-2 Main Protease Provides a Basis for Design of Improved  $\alpha$ -Ketoamide Inhibitors. *Science* **2020**, *368* (6489), 409–412. <https://doi.org/10.1126/science.abb3405>.
- (5) Sacco, M. D.; Ma, C.; Lagarias, P.; Gao, A.; Townsend, J. A.; Meng, X.; Dube, P.; Zhang, X.; Hu, Y.; Kitamura, N.; Hurst, B.; Tarbet, B.; Marty, M. T.; Kolocouris, A.; Xiang, Y.; Chen, Y.; Wang, J. Structure and Inhibition of the SARS-CoV-2 Main Protease Reveal Strategy for Developing Dual Inhibitors against M<sup>pro</sup> and Cathepsin L. *Sci. Adv.* **2020**, *6* (50), eabe0751. <https://doi.org/10.1126/sciadv.abe0751>.
- (6) Ampornnanai, K.; Meng, X.; Shang, W.; Jin, Z.; Rogers, M.; Zhao, Y.; Rao, Z.; Liu, Z.-J.; Yang, H.; Zhang, L.; O'Neill, P. M.; Samar Hasnain, S. Inhibition Mechanism of SARS-CoV-2 Main Protease by Ebselen and Its Derivatives. *Nat. Commun.* **2021**, *12* (1), 3061. <https://doi.org/10.1038/s41467-021-23313-7>.
- (7) Ferreira, J. C.; Fadl, S.; Villanueva, A. J.; Rabeh, W. M. Catalytic Dyad Residues His41 and Cys145 Impact the Catalytic Activity and Overall Conformational Fold of the Main SARS-CoV-2 Protease 3-Chymotrypsin-Like Protease. *Front. Chem.* **2021**, *9*.
- (8) El-Baba, T. J.; Lutomski, C. A.; Kantsadi, A. L.; Malla, T. R.; John, T.; Mikhailov, V.; Bolla, J. R.; Schofield, C. J.; Zitzmann, N.; Vakonakis, I.; Robinson, C. V. Allosteric Inhibition of the SARS-CoV-2 Main Protease: Insights from Mass Spectrometry Based Assays\*\*. *Angew. Chem. Int. Ed.* **2020**, *59* (52), 23544–23548. <https://doi.org/10.1002/anie.202010316>.
- (9) Ma, C.; Sacco, M. D.; Hurst, B.; Townsend, J. A.; Hu, Y.; Szeto, T.; Zhang, X.; Tarbet, B.; Marty, M. T.; Chen, Y.; Wang, J. Boceprevir, GC-376, and Calpain Inhibitors II, XII Inhibit SARS-CoV-2 Viral Replication by Targeting the Viral Main Protease. *Cell Res.* **2020**, *30* (8), 678–692. <https://doi.org/10.1038/s41422-020-0356-z>.
- (10) Fu, L.; Ye, F.; Feng, Y.; Yu, F.; Wang, Q.; Wu, Y.; Zhao, C.; Sun, H.; Huang, B.; Niu, P.; Song, H.; Shi, Y.; Li, X.; Tan, W.; Qi, J.; Gao, G. F. Both Boceprevir and GC376 Efficaciously Inhibit SARS-CoV-2 by Targeting Its Main Protease. *Nat. Commun.* **2020**, *11* (1), 4417. <https://doi.org/10.1038/s41467-020-18233-x>.
- (11) Xia, Z.; Sacco, M.; Hu, Y.; Ma, C.; Meng, X.; Zhang, F.; Szeto, T.; Xiang, Y.; Chen, Y.; Wang, J. Rational Design of Hybrid SARS-CoV-2 Main Protease Inhibitors Guided by the Superimposed Cocrystal Structures with the Peptidomimetic Inhibitors GC-376, Telaprevir, and Boceprevir. *ACS Pharmacol. Transl. Sci.* **2021**, *4* (4), 1408–1421. <https://doi.org/10.1021/acspsci.1c00099>.
- (12) Vuong, W.; Fischer, C.; Khan, M. B.; van Belkum, M. J.; Lamer, T.; Willoughby, K. D.; Lu, J.; Arutyunova, E.; Joyce, M. A.; Safiran, H. A.; Shields, J. A.; Young, H. S.; Nieman, J. A.; Tyrrell, D. L.; Lemieux, M. J.; Vederas, J. C. Improved SARS-CoV-2 M<sup>pro</sup> Inhibitors Based on Feline Antiviral Drug GC376: Structural Enhancements, Increased Solubility, and Micellar Studies. *Eur. J. Med. Chem.* **2021**, *222*, 113584. <https://doi.org/10.1016/j.ejmech.2021.113584>.
- (13) Ma, C.; Hu, Y.; Townsend, J. A.; Lagarias, P. I.; Marty, M. T.; Kolocouris, A.; Wang, J. Ebselen, Disulfiram, Carmofur, PX-

- 12, Tideglusib, and Shikonin Are Nonspecific Promiscuous SARS-CoV-2 Main Protease Inhibitors. *ACS Pharmacol. Transl. Sci.* **2020**, *3* (6), 1265–1277. <https://doi.org/10.1021/acspsci.0c00130>.
- (14) Mirza, U. A.; Cohen, S. L.; Chait, B. T. Heat-Induced Conformational Changes in Proteins Studied by Electrospray Ionization Mass Spectrometry. *Anal. Chem.* **1993**, *65* (1), 1–6. <https://doi.org/10.1021/ac00049a003>.
- (15) Laganowsky, A.; Clemmer, D. E.; Russell, D. H. Variable-Temperature Native Mass Spectrometry for Studies of Protein Folding, Stabilities, Assembly, and Molecular Interactions. *Annu. Rev. Biophys.* **2022**, *51* (1), 63–77. <https://doi.org/10.1146/annurev-biophys-102221-101121>.
- (16) McCabe, J. W.; Shirzadeh, M.; Walker, T. E.; Lin, C.-W.; Jones, B. J.; Wysocki, V. H.; Barondeau, D. P.; Clemmer, D. E.; Laganowsky, A.; Russell, D. H. Variable-Temperature Electrospray Ionization for Temperature-Dependent Folding/Refolding Reactions of Proteins and Ligand Binding. *Anal. Chem.* **2021**, *93* (1), 1–10. <https://doi.org/10.1021/acs.analchem.1c00001>.
- (17) Poltash, M. L.; McCabe, J. W.; Shirzadeh, M.; Laganowsky, A.; Clowers, B. H.; Russell, D. H. Fourier Transform-Ion Mobility-Orbitrap Mass Spectrometer: A Next-Generation Instrument for Native Mass Spectrometry. *Anal. Chem.* **2018**, *90* (17), 10472–10478. <https://doi.org/10.1021/acs.analchem.8b02463>.
- (18) Sipe, S. N.; Sanders, J. D.; Reinecke, T.; Clowers, B. H.; Brodbelt, J. S. Separation and Collision Cross Section Measurements of Protein Complexes Afforded by a Modular Drift Tube Coupled to an Orbitrap Mass Spectrometer. *Anal. Chem.* **2022**, *94* (26), 9434–9441. <https://doi.org/10.1021/acs.analchem.2c01653>.
- (19) Bush, M. F.; Hall, Z.; Giles, K.; Hoyes, J.; Robinson, C. V.; Rutolo, B. T. Collision Cross Sections of Proteins and Their Complexes: A Calibration Framework and Database for Gas-Phase Structural Biology. *Anal. Chem.* **2010**, *82* (22), 9557–9565. <https://doi.org/10.1021/ac1022953>.
- (20) *Native IM-Orbitrap MS: Resolving what was hidden | Elsevier Enhanced Reader.* <https://doi.org/10.1016/j.trac.2019.05.035>.
- (21) *Solution thermochemistry of concanavalin A tetramer conformers measured by variable-temperature ESI-IMS-MS | Elsevier Enhanced Reader.* <https://doi.org/10.1016/j.ijms.2019.06.004>.
- (22) Janin, J. Principles of Protein-Protein Recognition from Structure to Thermodynamics. *Biochimie* **1995**, *77* (7), 497–505. [https://doi.org/10.1016/0300-9084\(96\)88166-1](https://doi.org/10.1016/0300-9084(96)88166-1).
- (23) El-Baba, T. J.; Woodall, D. W.; Raab, S. A.; Fuller, D. R.; Laganowsky, A.; Russell, D. H.; Clemmer, D. E. Melting Proteins: Evidence for Multiple Stable Structures upon Thermal Denaturation of Native Ubiquitin from Ion Mobility Spectrometry-Mass Spectrometry Measurements. *J. Am. Chem. Soc.* **2017**, *139* (18), 6306–6309. <https://doi.org/10.1021/jacs.7b02774>.
- (24) Benesch, J. L. P.; Sobott, F.; Robinson, C. V. Thermal Dissociation of Multimeric Protein Complexes by Using Nanoelectrospray Mass Spectrometry. *Anal. Chem.* **2003**, *75* (10), 2208–2214. <https://doi.org/10.1021/ac034132x>.
- (25) Woodall, D. W.; Henderson, L. W.; Raab, S. A.; Honma, K.; Clemmer, D. E. Understanding the Thermal Denaturation of Myoglobin with IMS-MS: Evidence for Multiple Stable Structures and Trapped Pre-Equilibrium States. *J. Am. Soc. Mass Spectrom.* **2021**, *32* (1), 64–72. <https://doi.org/10.1021/jasms.0c00075>.
- (26) Cong, X.; Liu, Y.; Liu, W.; Liang, X.; Russell, D. H.; Laganowsky, A. Determining Membrane Protein-Lipid Binding Thermodynamics Using Native Mass Spectrometry. *J. Am. Chem. Soc.* **2016**, *138* (13), 4346–4349. <https://doi.org/10.1021/jacs.6b01771>.
- (27) Morrison, L. J.; Brodbelt, J. S. 193 Nm Ultraviolet Photodissociation Mass Spectrometry of Tetrameric Protein Complexes Provides Insight into Quaternary and Secondary Protein Topology. *J. Am. Chem. Soc.* **2016**, *138* (34), 10849–10859. <https://doi.org/10.1021/jacs.6b03905>.
- (28) O'Brien, J. P.; Li, W.; Zhang, Y.; Brodbelt, J. S. Characterization of Native Protein Complexes Using Ultraviolet Photodissociation Mass Spectrometry. *J. Am. Chem. Soc.* **2014**, *136* (37), 12920–12928. <https://doi.org/10.1021/ja505217w>.
- (29) Zhou, M.; Lantz, C.; A. Brown, K.; Ge, Y.; Paša-Tolić, L.; A. Loo, J.; Lermyte, F. Higher-Order Structural Characterisation of Native Proteins and Complexes by Top-down Mass Spectrometry. *Chem. Sci.* **2020**, *11* (48), 12918–12936. <https://doi.org/10.1039/D0SC04392C>.
- (30) N. Sipe, S.; S. Brodbelt, J. Impact of Charge State on 193 Nm Ultraviolet Photodissociation of Protein Complexes. *Phys. Chem. Chem. Phys.* **2019**, *21* (18), 9265–9276. <https://doi.org/10.1039/C9CP01144G>.
- (31) Macias, L. A.; Sipe, S. N.; Santos, I. C.; Bashyal, A.; Mehaffey, M. R.; Brodbelt, J. S. Influence of Primary Structure on Fragmentation of Native-Like Proteins by Ultraviolet Photodissociation. *J. Am. Soc. Mass Spectrom.* **2021**, *32* (12), 2860–2873. <https://doi.org/10.1021/jasms.1c00269>.
- (32) Mellott, D. M.; Tseng, C.-T.; Drelich, A.; Fajtová, P.; Chenna, B. C.; Kostomiris, D. H.; Hsu, J.; Zhu, J.; Taylor, Z. W.; Kocurek, K. I.; Tat, V.; Katzfuss, A.; Li, L.; Giardini, M. A.; Skinner, D.; Hirata, K.; Yoon, M. C.; Beck, S.; Carlin, A. F.; Clark, A. E.; Beretta, L.; Maneval, D.; Hook, V.; Frueh, F.; Hurst, B. L.; Wang, H.; Rauschel, F. M.; O'Donoghue, A. J.; de Siqueira-Neto, J. L.; Meek, T. D.; McKerrow, J. H. A Clinical-Stage Cysteine Protease Inhibitor Blocks SARS-CoV-2 Infection of Human and Monkey Cells. *ACS Chem. Biol.* **2021**, *16* (4), 642–650. <https://doi.org/10.1021/acscchembio.0c00875>.
- (33) Xue, X.; Yang, H.; Shen, W.; Zhao, Q.; Li, J.; Yang, K.; Chen, C.; Jin, Y.; Bartlam, M.; Rao, Z. Production of Authentic SARS-CoV M(pro) with Enhanced Activity: Application as a Novel Tag-Cleavage Endopeptidase for Protein Overproduction. *J. Mol. Biol.* **2007**, *366* (3), 965–975. <https://doi.org/10.1016/j.jmb.2006.11.073>.
- (34) Fort, K. L.; Dyachenko, A.; Potel, C. M.; Corradini, E.; Marino, F.; Barendregt, A.; Makarov, A. A.; Scheltema, R. A.; Heck, A. J. R. Implementation of Ultraviolet Photodissociation on a Benchtop Q Exactive Mass Spectrometer and Its Application to Phosphoproteomics. *Anal. Chem.* **2016**, *88* (4), 2303–2310. <https://doi.org/10.1021/acs.analchem.5b04162>.
- (35) Mehaffey, M. R.; Sanders, J. D.; Holden, D. D.; Nilsson, C. L.; Brodbelt, J. S. Multistage Ultraviolet Photodissociation Mass Spectrometry To Characterize Single Amino Acid Variants of Human Mitochondrial BCAT2. *Anal. Chem.* **2018**, *90* (16), 9904–9911. <https://doi.org/10.1021/acs.analchem.8b02099>.
- (36) Sanders, J. D.; Shields, S. W.; Escobar, E. E.; Lanzillotti, M. B.; Butalewicz, J. P.; James, V. K.; Blevins, M. S.; Sipe, S. N.; Brodbelt, J. S. Enhanced Ion Mobility Separation and Characterization of Isomeric Phosphatidylcholines Using Absorption Mode Fourier Transform Multiplexing and Ultraviolet Photodissociation Mass Spectrometry. *Anal. Chem.* **2022**, *94* (10), 4252–4259. <https://doi.org/10.1021/acs.analchem.1c04711>.
- (37) Reinecke, T.; Clowers, B. H. Implementation of a Flexible, Open-Source Platform for Ion Mobility Spectrometry. *HardwareX* **2018**, *4*, e00030. <https://doi.org/10.1016/j.ohx.2018.e00030>.
- (38) Reinecke, T.; Naylor, C. N.; Clowers, B. H. Ion Multiplexing: Maximizing Throughput and Signal to Noise Ratio for Ion Mobility Spectrometry. *TrAC Trends Anal. Chem.* **2019**, *116*, 340–345. <https://doi.org/10.1016/j.trac.2019.03.014>.

- (39) Greenfield, N. J. Using Circular Dichroism Spectra to Estimate Protein Secondary Structure. *Nat. Protoc.* **2006**, *1* (6), 2876–2890. <https://doi.org/10.1038/nprot.2006.202>.
- (40) Holzwarth, G.; Doty, P. The Ultraviolet Circular Dichroism of Polypeptides. *J. Am. Chem. Soc.* **1965**, *87* (2), 218–228. <https://doi.org/10.1021/ja01080a015>.
- (41) Marty, M. T.; Baldwin, A. J.; Marklund, E. G.; Hochberg, G. K. A.; Benesch, J. L. P.; Robinson, C. V. Bayesian Deconvolution of Mass and Ion Mobility Spectra: From Binary Interactions to Polydisperse Ensembles. *Anal. Chem.* **2015**, *87* (8), 4370–4376. <https://doi.org/10.1021/acs.analchem.5b00140>.
- (42) Juetten, K. J.; Brodbelt, J. S. MS-TAFI: A Tool for the Analysis of Fragment Ions Generated from Intact Proteins. *J. Proteome Res.* **2023**, *22* (2), 546–550. <https://doi.org/10.1021/acs.jproteome.2c00594>.
- (43) Butalewicz, J. P.; Sanders, J. D.; Clowers, B. H.; Brodbelt, J. S. Improving Ion Mobility Mass Spectrometry of Proteins through Tristate Gating and Optimization of Multiplexing Parameters. *J. Am. Soc. Mass Spectrom.* **2023**, *34* (1), 101–108. <https://doi.org/10.1021/jasms.2c00274>.
- (44) Turzo, S. B. A.; Seffernick, J. T.; Rolland, A. D.; Donor, M. T.; Heinze, S.; Prell, J. S.; Wysocki, V. H.; Lindert, S. Protein Shape Sampled by Ion Mobility Mass Spectrometry Consistently Improves Protein Structure Prediction. *Nat. Commun.* **2022**, *13* (1), 4377. <https://doi.org/10.1038/s41467-022-32075-9>.
- (45) Lyskov, S.; Chou, F.-C.; Conchúir, S. Ó.; Der, B. S.; Drew, K.; Kuroda, D.; Xu, J.; Weitzner, B. D.; Renfrew, P. D.; Sripakdeevong, P.; Borgo, B.; Havranek, J. J.; Kuhlman, B.; Kortemme, T.; Bonneau, R.; Gray, J. J.; Das, R. Serverification of Molecular Modeling Applications: The Rosetta Online Server That Includes Everyone (ROSIE). *PLOS ONE* **2013**, *8* (5), e63906. <https://doi.org/10.1371/journal.pone.0063906>.
- (46) Sanders, J. D.; Mullen, C.; Watts, E.; Holden, D. D.; Syka, J. E. P.; Schwartz, J. C.; Brodbelt, J. S. Enhanced Sequence Coverage of Large Proteins by Combining Ultraviolet Photodissociation with Proton Transfer Reactions. *Anal. Chem.* **2020**, *92* (1), 1041–1049. <https://doi.org/10.1021/acs.analchem.9b04026>.
- (47) Kneller, D. W.; Phillips, G.; O'Neill, H. M.; Jedrzejczak, R.; Stols, L.; Langan, P.; Joachimiak, A.; Coates, L.; Kovalevsky, A. Structural Plasticity of SARS-CoV-2 3CL Mpro Active Site Cavity Revealed by Room Temperature X-Ray Crystallography. *Nat. Commun.* **2020**, *11* (1), 3202. <https://doi.org/10.1038/s41467-020-16954-7>.
- (48) Nashed, N. T.; Aniana, A.; Ghirlando, R.; Chiliveri, S. C.; Louis, J. M. Modulation of the Monomer-Dimer Equilibrium and Catalytic Activity of SARS-CoV-2 Main Protease by a Transition-State Analog Inhibitor. *Commun. Biol.* **2022**, *5* (1), 1–9. <https://doi.org/10.1038/s42003-022-03084-7>.
- (49) Morrison, L. J.; Brodbelt, J. S. Charge Site Assignment in Native Proteins by Ultraviolet Photodissociation (UVPD) Mass Spectrometry. *The Analyst* **2016**, *141* (1), 166–176. <https://doi.org/10.1039/c5an01819f>.
- (50) Zhou, M.; Liu, W.; Shaw, J. B. Charge Movement and Structural Changes in the Gas-Phase Unfolding of Multimeric Protein Complexes Captured by Native Top-Down Mass Spectrometry. *Anal. Chem.* **2019**. <https://doi.org/10.1021/acs.analchem.9b03469>.
- (51) Loo, R. R. O.; Loo, J. A. Salt Bridge Rearrangement (SaBRE) Explains the Dissociation Behavior of Noncovalent Complexes. *J. Am. Soc. Mass Spectrom.* **2016**, *27* (6), 975–990. <https://doi.org/10.1007/s13361-016-1375-3>.
- (52) Jang, H.; Hall, C. K.; Zhou, Y. Thermodynamics and Stability of a  $\beta$ -Sheet Complex: Molecular Dynamics Simulations on Simplified off-Lattice Protein Models. *Protein Sci. Publ. Protein Soc.* **2004**, *13* (1), 40–53. <https://doi.org/10.1110/ps.03162804>.
- (53) Jayaraman, G.; Kumar, T. K. S.; Sivaraman, T.; Lin, W. Y.; Chang, D. K.; Yu, C. Thermal Denaturation of an All  $\beta$ -Sheet Protein — Identification of a Stable Partially Structured Intermediate at High Temperature. *Int. J. Biol. Macromol.* **1996**, *18* (4), 303–306. [https://doi.org/10.1016/0141-8130\(95\)01088-2](https://doi.org/10.1016/0141-8130(95)01088-2).
- (54) Vijayakumar, S.; Vishveshwara, S.; Ravishanker, G.; Beveridge, D. L. Differential Stability of Beta-Sheets and Alpha-Helices in Beta-Lactamase: A High Temperature Molecular Dynamics Study of Unfolding Intermediates. *Biophys. J.* **1993**, *65* (6), 2304–2312. [https://doi.org/10.1016/S0006-3495\(93\)81288-8](https://doi.org/10.1016/S0006-3495(93)81288-8).
- (55) Fersht, A.; Fersht, U. A. *Structure and Mechanism in Protein Science: A Guide to Enzyme Catalysis and Protein Folding*; Macmillan, 1999.
- (56) Dai, W.; Zhang, B.; Jiang, X.-M.; Su, H.; Li, J.; Zhao, Y.; Xie, X.; Jin, Z.; Peng, J.; Liu, F.; Li, C.; Li, Y.; Bai, F.; Wang, H.; Cheng, X.; Cen, X.; Hu, S.; Yang, X.; Wang, J.; Liu, X.; Xiao, G.; Jiang, H.; Rao, Z.; Zhang, L.-K.; Xu, Y.; Yang, H.; Liu, H. Structure-Based Design of Antiviral Drug Candidates Targeting the SARS-CoV-2 Main Protease. *Science* **2020**, *368* (6497), 1331–1335. <https://doi.org/10.1126/science.abb4489>.
- (57) Agost-Beltrán, L.; de la Hoz-Rodríguez, S.; Bou-Iserte, L.; Rodríguez, S.; Fernández-de-la-Pradilla, A.; González, F. V. Advances in the Development of SARS-CoV-2 Mpro Inhibitors. *Molecules* **2022**, *27* (8), 2523. <https://doi.org/10.3390/molecules27082523>.

